IEEE Access
Multidisciplinary | Rapid Review | Open Access Journal

Received March 11, 2019, accepted April 9, 2019, date of publication April 29, 2019, date of current version May 22, 2019.

*Digital Object Identifier 10.1109/ACCESS.2019.2913702*

# Sliding-Mode-Observer-Based Position Estimation for Sensorless Control of the Planar Switched Reluctance Motor

**JUNDI SUN[1,2], (Student Member, IEEE), GUANG-ZHONG CAO[1], (Senior Member, IEEE), SU-DAN HUANG[1], (Member, IEEE), YEPING PENG[1], (Member, IEEE), JIANGBIAO HE[3], (Senior Member, IEEE), and QING-QUAN QIAN[2]**

[1]Shenzhen Key Laboratory of Electromagnetic Control, Shenzhen University, Shenzhen 518060, China
[2]College of Electrical Engineering, Southwest Jiaotong University, Chengdu 610031, China
[3]Department of Electrical and Computer Engineering, University of Kentucky, Lexington, KY 40517, USA

Corresponding authors: Guang-Zhong Cao (gzcao.01@gmail.com) and Su-Dan Huang (hsdsudan@gmail.com)

This work was supported in part by the National Natural Science Foundation of China under Grant NSFC 51677120 and NSFC U1813212, in part by the Natural Science Foundation of Guangdong Province, China, under Grant 2017A030310460 and Grant 2018A030310522, in part by the Shenzhen Government Fund under Grant 20170919104246276 and Grant JCYJ20180305124348603, and in part by the Fundamental Research Funds for the Shenzhen University under Grant 2017039.

**ABSTRACT** This paper proposes a position estimation method for a planar switched reluctance motor (PSRM). In the method, a second-order sliding mode observer (SMO) is used to achieve sensorless control of a PSRM for the first time. A sensorless closed-loop control strategy based on the SMO without a position sensor for the PSRM is constructed. The SMO mainly consists of a flux linkage estimation, an adaptive current estimation, an observing error calculation, and a position estimation section. An adaptive current observer is applied in the current estimation section to minimize the error between the measured and estimated currents and to increase the accuracy of the position estimation. The flux linkage is estimated by the voltage equation of the PSRM, and the estimated flux linkage is then used to estimate the phase current in the adaptive current observer. To calculate the observing error of the SMO using the measured and estimated phase currents, the observing error of the thrust force is introduced to replace the immeasurable state error of the position and speed of the mover. The sliding surface is designed based on the error of the thrust force, and stability analysis is given. Once the sliding surface is reached, the mover position is then estimated accurately. Finally, the effectiveness of the proposed method for the PSRM is verified experimentally.

**INDEX TERMS** Position estimation, planar switched reluctance motor (PSRM), sensorless control, sliding mode observer (SMO).

## I. INTRODUCTION

Direct-drive planar motors have gained increasing attention in the advanced manufacturing industry because of their advantages of direct drive, simple structure, high reliability, low friction, and no backlash compared with conventional planar motors with cumbersome mechanical transmission mechanisms [1]–[4]. Among the different kinds of planar motors, the planar switched reluctance motor (PSRM) is an attractive candidate in two-dimensional (2-D) positioning devices because it features high precision, low cost, low heat loss, easy manufacturing, and strong resilience to harsh environments [5]–[6]. A variety of research studies on PSRMs have been reported over the past decade. An inverse force function using sparse least squares support vector machines (LS-SVMs) was proposed in [7] to achieve nonlinear modeling for precision motion of a PSRM. An improved PSRM using an optimization design was developed in [8] to minimize the electromagnetic force ripple. An adaptive controller was applied to a PSRM in [9], and the experimental results showed that the controller had better position control performance than a proportional integral derivative (PID) algorithm in dynamic index, static index, and robustness to disturbances. A theoretical and experimental study of an efficiency

The associate editor coordinating the review of this manuscript and approving it for publication was Gaolin Wang.

improvement for a PSRM was performed, which employed a novel current distribution method with a maximum-force-per-ampere strategy [6]. A position detection approach to achieve sensorless control of a PSRM using a current injection method was proposed in [10], and the effectiveness of sensorless position detection was verified through simulation.

For precision control of a PSRM, accurate mover position feedback is essential, which can be obtained via direct position sensors or indirect sensorless control methods. Direct position sensors, such as linear optical encoders or magnetic scales, offer accurate position signals continuously; however, they result in higher cost, a more complicated system structure, and lower system reliability. To avoid this issue, developing a sensorless control method, which features a lower cost, a less complicated system structure, and higher system reliability, is effective for the PSRM.

However, few studies have comprehensively reported sensorless control of a PSRM thus far. Over the past three decades, multifarious sensorless control methods have been proposed to eliminate the position sensors for rotary switched reluctance motors (RSRMs), e.g., impressed diagnostic pulse-voltage methods [11]–[12], modulation-based methods [13]–[14], current waveform monitoring methods [15]–[19], flux/current methods [20], neural-network-based methods [21]–[22], fuzzy-logic-based methods [23]–[24], and state observer methods [25]–[27].

Among these sensorless control methods, the impressed diagnostic pulse-voltage method, the flux/current method, and the state observer method are more feasible in terms of realizing sensorless control of a PSRM. The flux/current method takes advantage of the inherent flux/current magnetic characteristics to infer the mover position from the measurement data of the current and the flux [20]. There are three drawbacks if this method is applied to a PSRM: 1) the number of the stator poles for a PSRM is usually much larger than that for an RSRM; thus, it is difficult to guarantee the same flux-current-position profile for all pole pitches of the mover and stator because of manufacturing error; 2) a large memory storage is needed to store precision flux-current-position data; 3) the detected current is usually susceptible to noise caused by the drivers, which will result in a large error for the position estimation. The impressed diagnostic pulse-voltage method probes an unexcited phase with a short-duration voltage pulse and evaluates the resulting current to measure the mover position [12], [28]. However, a nonnegligible opposite force is generated by the diagnostic pulse when the PSRM operates at high speed; thus, this method is only applicable for initial and low-speed position estimations. The state observer method is commonly categorized as the Luenberger observer and the sliding mode observer (SMO). Both approaches employ the operating current and voltage to calculate the mover position. The Luenberger observer is computationally intensive, and the linear Luenberger observer is sensitive to parameter changes. Since the PSRM is magnetically saturated under a heavy load condition, the stability and robustness of the Luenberger observer are unsatisfactory. The SMO has good adaptability and robustness to interior nonlinear and external disturbances. Furthermore, this method has the advantage of generating zero opposite force without an injected pulse [12]. As mentioned above, the SMO is the desired method for sensorless control of a PSRM.

The PSRM, like the RSRM, is developed based on the minimum reluctance principle; nevertheless, it is different and challenging to apply the SMO in a PSRM because the PSRM has three disadvantages with regard to position estimation compared with the RSRM.

1) Higher requirements for accuracy and the calculation. Most RSRMs operate under speed control mode, while the PSRM is usually applied in position control mode. Position estimation for RSRMs usually only requires several discrete position signals for speed estimation, while for a PSRM, the estimated position information is required to be continuous and more precise for real-time position feedback and phase inductance calculations. Therefore, the accuracy requirement for the position estimation for a PSRM is much higher than that of an RSRM. Moreover, the real-time capability requirement of the system is also higher, as the SMO is computationally intensive and a continuous estimation results in a larger calculation than that required for an RSRM.

2) Smaller variation in the inductance. The SMO utilizes inductance variation information to determine the position on account of the phase inductance of the RSRM varying significantly with the rotor position. The ratio of the maximum to minimum inductance in an RSRM is generally three or even larger, while that of the proposed PSRM is only approximately 1.2 owing to a smaller pole pitch of the PSRM. The inductance-position curve is generally measured offline based on the assumption that the air gap is constant. Actually, the air gap varies due to the attraction force when the machine is running. For an RSRM, the attraction force can be balanced due to the symmetrical structure, while in the case of a PSRM, the attraction force directly acts downward on the moving platform, causing the variation in the air gap. Due to the small ratio of the maximum to minimum inductance, a small variation in the air gap will lead to a large position estimation error for the PSRM. This indicates that the sensitivity of the inductance to position for a PSRM is much lower than that of an RSRM, and the position estimation accuracy is easily affected by the air gap.

3) Non-periodical characteristic. Theoretically, the current-inductance-position curves are the same at each pitch in an RSRM and a PSRM. Actually, due to the factor of processing, the current-inductance-position curve in each pitch is different. The number of stator poles in an RSRM is usually 6, 8, or 12, while that in a PSRM is generally more than 100. Compared to RSRMs, it is impossible for a PSRM to measure the current-inductance-position curves of every pole pitch. Therefore, PSRMs suffers more from the non-periodical characteristic than RSRMs.

In this paper, an SMO-based position estimation method is proposed to achieve sensorless control of a PSRM. The contributions and novelty of this paper consist of the following:

i) developing an SMO for a PSRM to achieve sensorless control for the first time; ii) extending the sensorless control study to a PSRM.

The organization of the remainder of the paper is as follows. The mathematical model of the PSRM is given in section II. The proposed position estimation method is clarified in section III. The experimental setup, results, and analysis are given in section IV. Section V concludes the paper.

**TABLE 1. Specifications of the PSRM.**

| Parameters | Value |
|---|---|
| Pole pitch of the movers and stators | 7.2 mm |
| Tooth width of the movers and stators | 3.6 mm |
| Air gap | 0.3 mm |
| Stroke of the motor | 170 mm (x) ×290 mm (y) |
| Mass of the x-axis moving platform | 5.9 kg |
| Mass of the y-axis moving platform | 13.9 kg |
| Phase resistance | 0.5 Ω |
| Number of turns per phase | 150 |

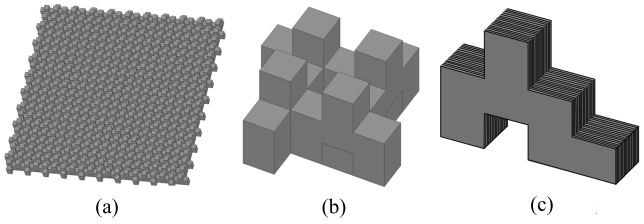


**FIGURE 1. Structure of stator sets, combination of four stator blocks and one stator block. (a) Stator sets. (b) Four stator blocks. (c) Stator block.**

## II. MATHEMATICAL MODEL OF THE PSRM

The proposed PSRM is a two-dimensional motor that can be considered as two linear switched reluctance motors with orthogonal magnetic circuits [8]. The prototype of the PSRM developed in our laboratory is presented in [6]. The specifications of the PSRM are listed in Table 1. This PSRM comprises two components: 1) a stator platform and 2) a moving platform. The stator platform consists of a stator base, stator sets, a y-axis linear guide and a y-axis linear encoder on the stator base. The stator sets are the combination of four stator blocks laminated with 0.3 mm silicon steel plates, as shown in Fig. 1. The moving platform consists of a y-axis moving platform, an x-axis linear guide, an x-axis moving platform on the y-axis moving platform, and an x-axis linear encoder. Two sets of three-phase movers are installed on the $x$-axis moving platform perpendicular to each other, as shown in Fig. 2(a). The movers are laminated with 0.3 mm silicon steel plates with three-phase coils, as shown in Fig. 2(b)-(c). Due to the perpendicular arrangement, the two sets of three-phase wingdings are decoupled magnetically. Phases xa, xb, and xc are responsible for motion in the x-axis, and phases ya, yb, and yc are responsible for motion in the y-axis.

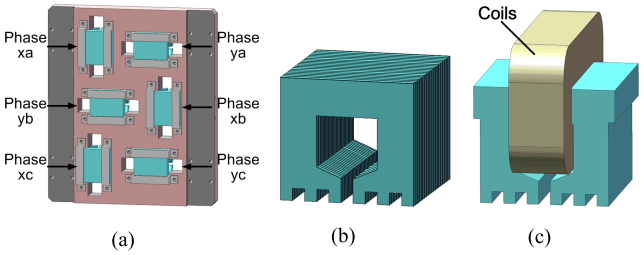


**FIGURE 2. Structure of the x-axis moving platform and the mover. (a) $x$-axis moving platform. (b) Silicon steel plates. (c) Mover.**

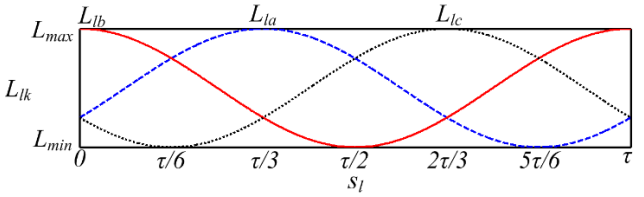


**FIGURE 3. Phase inductance versus mover position of $l$-axis.**

The mathematical model of the PSRM under the assumption of magnetic linearity can be represented as

$$\dot{\psi}_{lk} = U_{lk} - i_{lk}R_{lk} \tag{1}$$

$$\dot{v}_l = -\frac{B}{m_l}v_l + \frac{1}{m_l}(f_l - f_L) \tag{2}$$

$$\dot{s}_l = v_l \tag{3}$$

$$f_l = \sum_{k=a}^{c} \frac{1}{2}\frac{\partial L_{lk}}{\partial s} i_{lk}^2 \tag{4}$$

where $\psi_{lk}$, $U_{lk}$, $i_{lk}$, $R_{lk}$, and $L_{lk}$ are the flux linkage, the phase voltage, the phase current, the resistance, and the inductance of phase $k$ ($k$ = a, b, c) in the $l$-axis ($l$ = x, y), respectively. $s_l$ and $v_l$ are the mover position and mover speed in the $l$-axis, respectively. Define the position where the salient pole of the mover completely aligns with the salient pole of the stator as the origin position. $f_l$ is the electromagnetic thrust force in the $l$-axis, and $f_L$ is the external load force. $B$ is the viscous damping coefficient, and $m_l$ is the mass of the moving platform. The phase flux linkage $\psi_{lk}$, the mover position $s_l$, and the mover speed $v_l$ constitute the state variables. When the fringe effect and saturation effect that lead to the magnetic nonlinearity are neglected, the phase inductance of the PSRM linearly varies with the mover position for a given current [29], as shown in Fig. 3. The inductance in the $l$-axis is assumed to be given by

$$\begin{cases} L_{la}(s_l(t)) = L_s + L_o - L_\Delta \cos(\dfrac{2\pi s_l(t)}{\tau} + \dfrac{\pi}{3}) \\ L_{lb}(s_l(t)) = L_s + L_o + L_\Delta \cos(\dfrac{2\pi s_l(t)}{\tau}) \\ L_{lc}(s_l(t)) = L_s + L_o - L_\Delta \cos(\dfrac{2\pi s_l(t)}{\tau} - \dfrac{\pi}{3}) \end{cases} \tag{5}$$

where $\tau$ is the pole distance. $L_s$, $L_o$, and $L_\Delta$ are the leakage inductance, average inductance, and variation in the inductance in the $l$-axis, respectively. Rearranging (4) with (5),

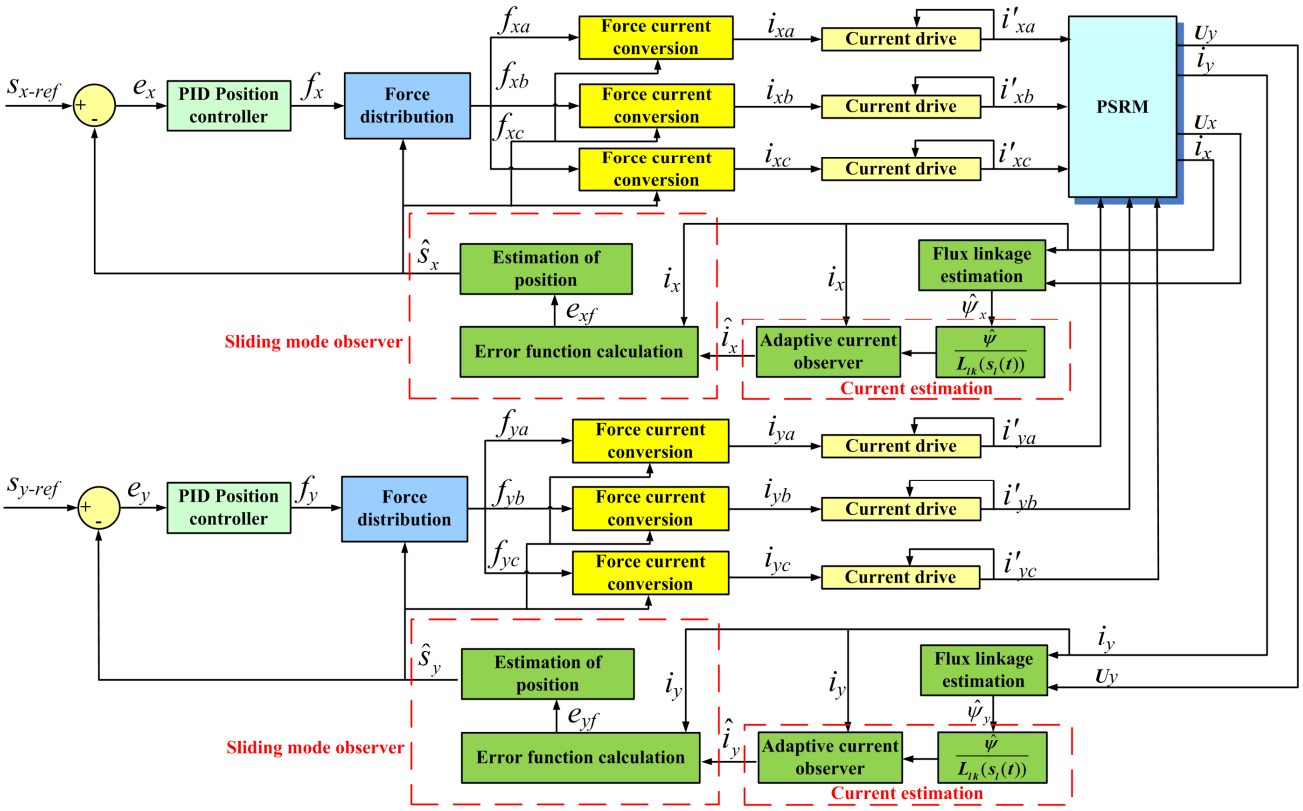


**FIGURE 4.** Position sensorless control of the PSRM system based on the sliding mode observer.

the thrust force can be expressed as

$$\begin{cases} f_{la}(t) = \dfrac{\pi L_\Delta i_{la}^2 \sin(\dfrac{2\pi s_l(t)}{\tau} + \dfrac{\pi}{3})}{\tau} \\ f_{lb}(t) = -\dfrac{\pi L_\Delta i_{lb}^2 \sin(\dfrac{2\pi s_l(t)}{\tau})}{\tau} \\ f_{lc}(t) = \dfrac{\pi L_\Delta i_{lc}^2 \sin(\dfrac{2\pi s_l(t)}{\tau} - \dfrac{\pi}{3})}{\tau} \end{cases} \tag{6}$$

$L_o$ and $L_\Delta$ are given by

$$L_o = \frac{L_{\max} + L_{\min}}{2} \tag{7}$$

$$L_\Delta = \frac{L_{\max} - L_{\min}}{2} \tag{8}$$

where $L_{\max}$ is the inductance of the mover coil when the mover is at the aligned position, which is the maximum inductance. $L_{\min}$ is the inductance of the mover coil when the mover is at the unaligned position, which is the minimum inductance.

## III. PROPOSED SLIDING-MODE-OBSERVER-BASED POSITION ESTIMATION METHOD

### A. SENSORLESS CONTROL STRATEGY

Fig. 4 depicts the position sensorless control drive system of the PSRM based on the SMO. The force distribution control method is applied to generate the desired thrust force with a low ripple. The outer loop of the control system is the position loop, and the inner loop is the current loop. The output of the position controller is a given thrust force, and the thrust force is assigned to the thrust force distribution function to obtain the given thrust force and current of each phase.

For linear motion in the x-axis, the mover position is estimated by the SMO algorithm. $\hat{S}_x$ is compared with the reference position $s_{x-ref}$, and the position error $e_x$ is processed to produce the thrust force command $f_x$ via an x-axis PID controller. In terms of $f_x$ and $\hat{S}_x$, the three-phase current commands $i_{xa}$, $i_{xb}$, and $i_{xc}$ are obtained from the force current conversion algorithm.$i_{xa}$,$i_{xb}$, $i_{xc}$, and the detected three-phase currents $i'_{xa}$, $i'_{xb}$, $i'_{xc}$are processed via the current drive to provide three-phase currents to the PSRM for achieving x-axis motion. The y-axis operates on the same principle as the x-axis.

In the SMO algorithm, the measured three-phase currents and voltages are utilized to calculate the flux linkage according to the phase voltage equation. The phase currents are then estimated based on the flux linkage and the inductance model of the PSRM. In this paper, an adaptive current estimation algorithm is applied to minimize the effect of current noise and to increase the precision of the position estimation. Comparing the estimated currents with the ones measured by the current drive, the error is then used to estimate the position of the mover by the observer.

### B. ADAPTIVE CURRENT ESTIMATION

The measured variables in the sensorless PSRM drive system are the phase current $i_{lk}$ and the phase voltage $U_{lk}$. In the SMO, the measured phase current $i_{lk}$ and the estimated phase current $\hat{i}_{lk}$ are used to calculate the observing errors. Neglecting the saturation nonlinearity, the estimated initial current $\hat{i}_0$ is given as

$$\hat{i}_0 = \frac{\hat{\psi}_0}{L_{lk}\,(s_l(t))} \tag{9}$$

where $\hat{\psi}_0$ is the initial flux linkage of phase $k$ in the $l$-axis in each cycle. To reduce the estimation error of the current at each subsequent moment, a PI adaptive observer is used to improve the current estimation accuracy,

$$\hat{i}_{n+1} = \frac{\hat{\psi}_{n+1}}{L_{lk}(s_l(t))} + k_p(i_{n+1} - \hat{i}_n) + k_i \int (i_{n+1} - \hat{i}_n)dt \tag{10}$$

where $k_p$ and $k_i$ are the proportional and integral coefficients of the PI controller, respectively.

### C. SLIDING-MODE-OBSERVER-BASED POSITION ESTIMATION

The phase flux linkage is computed by the integration of (1) as

$$\hat{\psi}_{lk} = \int (U_{lk} - i_{lk}R_{lk})dt \tag{11}$$

on the assumption that the error in the state variable $\psi_{lk}$ is zero.

The viscous damping coefficient $B$ in (2) is much smaller than the mass of the mover $m_l$, so (2) can be rearranged as

$$\dot{v}_l = \frac{1}{m_l}(\hat{f}_l - f_L). \tag{12}$$

Therefore, a reduced observer for the PSRM model is designed. The second-order SMO can be configured as

$$\dot{\hat{s}}_l = \hat{v}_l + k_{ls}sigmoid(e_{ls}) \tag{13}$$

$$\dot{\hat{v}}_l = \frac{1}{m_l}(\hat{f}_l - f_L) + k_{lv}sigmoid(e_{lv}) \tag{14}$$

where $\hat{S}_l$ and $\hat{v}_l$ are the estimated mover position and the estimated mover speed in the $l$-axis, respectively. $k_{ls}$ and $k_{lv}$ are the observer gains. The sigmoid function is applied to reduce chattering instead of the sign function, which is nonlinear [31]–[33].

Define the observing errors as

$$e_{ls} = s_l - \hat{s}_l \tag{15}$$

$$e_{lv} = v_l - \hat{v}_l. \tag{16}$$

However, the state variables $s_l$ and $v_l$ are immeasurable in this sensorless PSRM drive system. As a result, $e_{ls}$ and $e_{lv}$ are also not measurable. In this paper, the observing error of the thrust force $e_{lf}$ is introduced to replace $e_{ls}$ and $e_{lv}$. $e_{lf}$ is configured as

$$e_{lf} = \sum_{k=a}^{c}(f_{lk} - \hat{f}_{lk}) \tag{17}$$

where $f_{lk}$ is the thrust force of phase $k$ in the $l$-axis. It must be noted that the thrust force $f_l$ is equivalent to the load force $f_{L,}$ while the PSRM system is working on the sliding mode surface

$$S_{ls} = e_{ls} = s_l - \hat{s}_l = 0 \tag{18}$$

i.e., $e_{lf}$ is now zero. Hence, if the thrust force increases at this time ($e_{lf} > 0$), the mover will consequently accelerate, causing the position estimated error $e_{lv}$ and the speed estimated error $e_{ls}$ to increase to greater than 0. If the thrust force decreases rather than increases at this time ($e_{lf} < 0$), the mover will decelerate, causing $e_{lv}$ and $e_{ls}$ to decrease to smaller than 0. It can be concluded that

$$\mathrm{sgn}(e_{lf}) = \mathrm{sgn}(e_{ls}) = \mathrm{sgn}(e_{lv}). \tag{19}$$

Therefore, the indirect sliding surface

$$e_{lf} = \sum_{k=a}^{c}(f_{lk} - \hat{f}_{lk}) = 0 \tag{20}$$

may be used to substitute the desired sliding surface $e_{ls} = 0$. This means that it is reasonable to select $e_{lf}$ to be a substitution of $e_{lv}$ and $e_{ls}$. Then, the observer is represented as

$$\dot{\hat{s}}_l = \hat{v}_l + k_{ls}sigmoid(e_{lf}) \tag{21}$$

$$\dot{\hat{v}}_l = \frac{1}{m_l}(\hat{f}_l - f_L) + k_{lv}sigmoid(e_{lf}) \tag{22}$$

Define the Lyapunov function

$$V = \frac{1}{2}S_{ls}^2. \tag{23}$$

The differential equation of $V$ is

$$\dot{V} = S_{ls} \cdot \dot{S}_{ls} = e_{ls}(e_{lv} - k_{ls}sigmoid\ (e_{lf})). \tag{24}$$

The reaching and stability conditions are satisfied for any initial values of the states as long as the following inequality is true:

$$\dot{V} = e_{ls}(e_{lv} - k_{ls}sigmoid(e_{lf})) < 0 \tag{25}$$

This condition is satisfied provided that

$$k_{ls} > |e_{lv}| \tag{26}$$

which guarantees that the sliding surface will be reached.

From (13) to (16), the errors of the SMO are defined as

$$\dot{e}_{ls} = e_{lv} - k_{ls}sigmoid(e_{lf}) \tag{27}$$

$$\dot{e}_{lv} = \frac{1}{m_l}(f_l - \hat{f}_l) - k_{lv}sigmoid(e_{lf}). \tag{28}$$

The first term on the right side of (28) can be neglected, as the difference between the actual and estimated thrust force is a small number, $k_{lv}$ is typically a much larger number. Then, the first term on the right side can be neglected and $\dot{e}_{lv}$ becomes

$$\dot{e}_{lv} = -k_{lv}sigmoid(e_{lf}). \tag{29}$$

On the sliding surface $S_{ls} = 0$, the average value of $\dot{e}_{ls}$ can be considered 0, which gives from (27)

$$e_{lv} = k_{ls}sigmoid(e_{lf}) \tag{30}$$

**TABLE 2. The parameters of the SMO and the PI parameters of the adaptive current estimation.**

| Quantity | x-axis | y-axis |
|---|---|---|
| SMO parameters | $k_{xv}$= 53.5 | $k_{yv}$= 50 |
| | $k_{xs}$= 343 | $k_{ys}$= 300 |
| PI parameters of the adaptive current estimation | $k_{p(xa)}$= 0.3, $k_{i(xa)}$= 1 | $k_{p(ya)}$= 0.3, $k_{i(ya)}$= 1 |
| | $k_{p(xb)}$= 0.4, $k_{i(xb)}$= 1 | $k_{p(yb)}$= 0.5, $k_{i(yb)}$= 1 |
| | $k_{p(xc)}$= 0.6, $k_{i(xc)}$= 1 | $k_{p(yc)}$= 0.6, $k_{i(yc)}$= 1 |

and then (29) can be rewritten as

$$\dot{e}_{lv} = -\frac{k_{lv}}{k_{ls}} e_{lv}. \tag{31}$$

Therefore, the speed error converges exponentially to zero on the assumption that condition (26) is met.

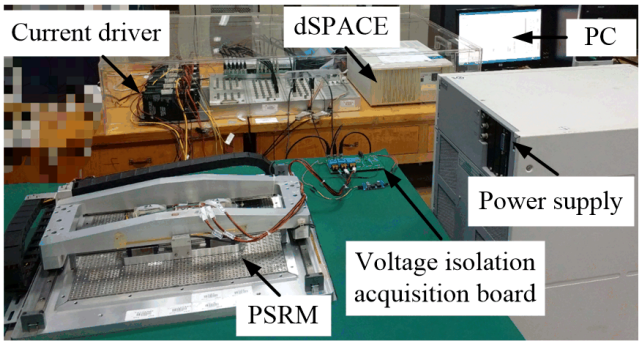


**FIGURE 5.** Experimental setup of the PSRM.

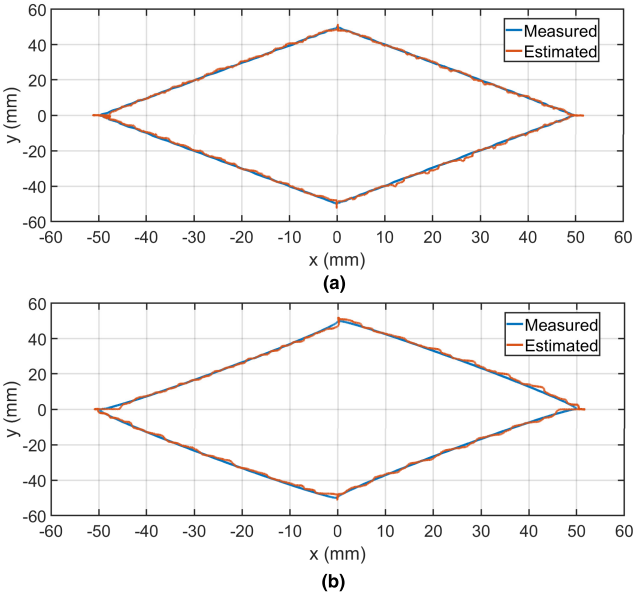


**FIGURE 6.** Experiment results of planar motion. (a) T = 10 s. (b) T = 15 s.

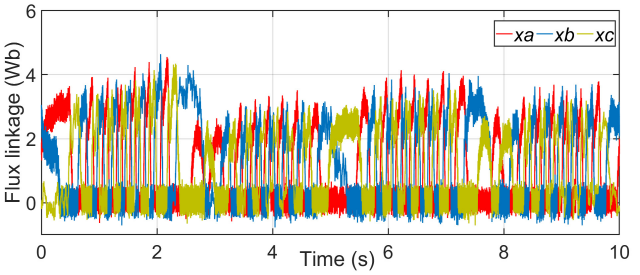


**FIGURE 7.** Estimated flux linkage without adaptive current estimation.

## IV. EXPERIMENTAL VERIFICATION AND ANALYSIS

### A. EXPERIMENTAL SETUP

Based on the dSPACE loop simulation platform, a position sensorless control experimental platform for the PSRM is built. The experimental platform consists of a PSRM with a power supply, a computer, a dSPACE module, a current drive, and a voltage isolation acquisition board, as shown in Fig. 5. The control algorithm is designed based on MATLAB/Simulink, and it is uploaded to the dSPACE modular hardware for realizing real-time control. The position estimation is realized with a sensor associated operation in this paper. Two linear optical encoders with dual resolutions of 50 nm and 100 nm are used to detect the actual positions, which is the foundation for the operation and commutation of the PSRM.

The voltage and current of the mover coil are obtained in real time by the voltage isolation acquisition board and the current drive. Furthermore, to reduce the effect of the offset voltage and noise in the voltage and current sampling process, an offset correction program and a low-pass filter with a cutoff frequency of 200 Hz are employed. These real-time voltage and current data are input to the SMO for position estimation.

### B. EXPERIMENTAL RESULTS

The parameters of the SMO and the PI parameters of the adaptive current estimation are given in Table 2. The experiment is designed to drive the PSRM to make a planar motion, which can be disassembled into trajectories in the x- and y-axes. These trajectories have an amplitude of 50 mm, and the planar trajectory experimental results with different duties (T = 10 s and T = 15 s) are shown in Fig. 6. The planar motion with a duty T of 10 s is split into the x- and y-axes for analysis. The estimated current and mover position of the x-axis are shown in Figs. 7-12, and the experimental results in the y-axis are shown in Figs. 13-16.

Fig. 7 shows the calculated flux linkage in every phase, and Fig. 8 shows the estimated current in the x-axis without adaptive current estimation. The current estimated error of phase xa ranges from −5.026 A to 2.339 A, and the average current absolute error is 0.547 A. The current estimated error of phase xb is from −2.474 A to 1.746 A, and the average current absolute error is 0.338 A. The current estimated error

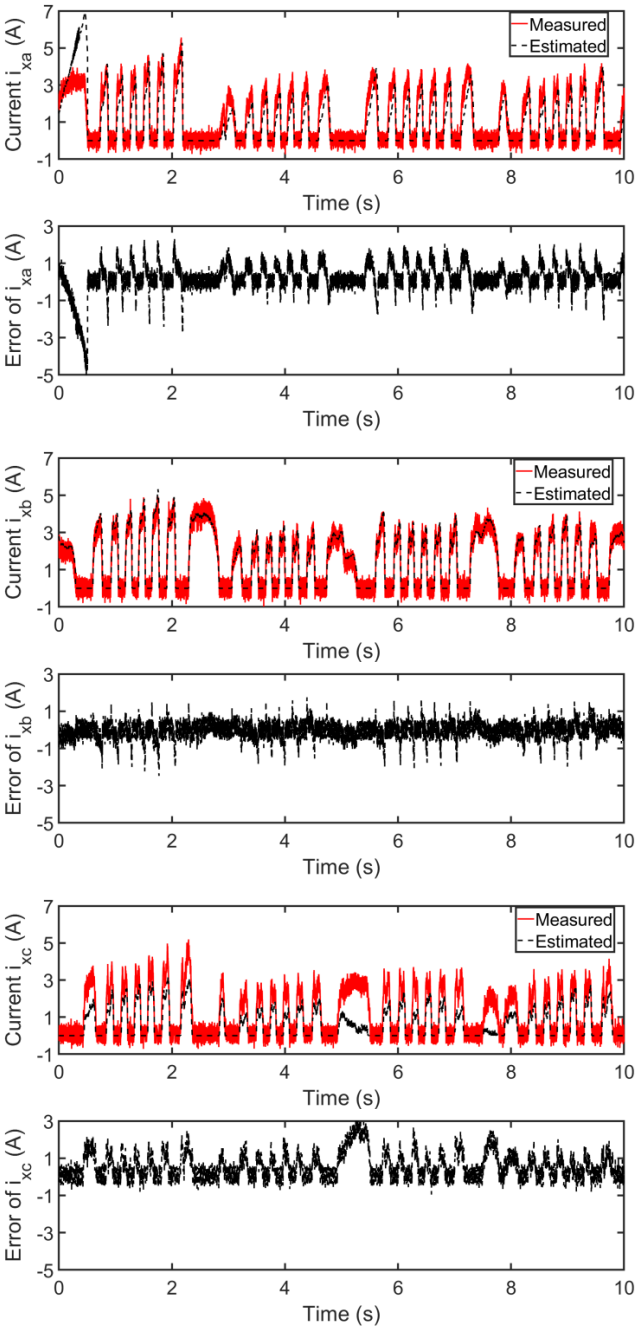


**FIGURE 8.** Estimated current results and estimated errors without adaptive current estimation in the x-axis.

of phase xc is from −0.956 A to 3.176 A, and the average current absolute error is 0.673 A.

Fig. 9 shows the estimated flux linkage, and Fig. 10 shows the estimated current in the x-axis with adaptive current estimation. The current estimated error of phase xa ranges from −1.853 A to 0.867 A, and the average current absolute error is 0.222 A. The current error of phase xb is from −1.157 A to 1.008 A, and the average current absolute error is 0.201 A. The current estimated error of phase xc is from −0.782 A to 1.081 A, and the average current absolute error

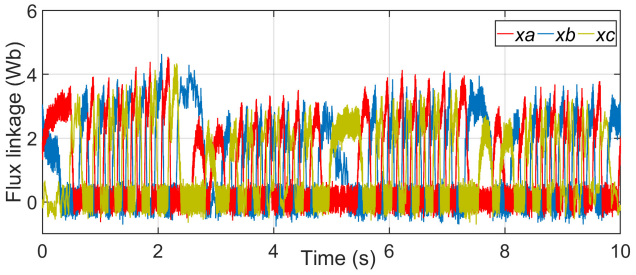


**FIGURE 9.** Estimated flux linkage with the adaptive current estimation.

is 0.215 A. Compared with the situation in which adaptive current estimation is not applied, the maximum errors of the current estimation of phases xa, xb, and xc are reduced by 63.1%, 59.3%, and 66.0%, respectively.

Fig. 11 shows the position estimation results in the x-axis without adaptive current estimation, and Fig. 12 shows the position estimation results when adaptive current estimation is applied. Without adaptive current estimation, the error between the measured position and the estimated position ranges from −3.014 mm to 6.642 mm, and the absolute position error is 2.483 mm on average. With adaptive current estimation, the position estimating error ranges from −2.239 mm to 1.785 mm, and the absolute position error is 0.885 mm on average. Compared with the situation in which adaptive current estimation is not applied, the maximum position estimated error is reduced by 66.3%.

Fig. 13 shows the estimated current in the y-axis without adaptive current estimation. The current estimated error of phase ya ranges from −0.742 A to 3.531 A, and the average current absolute error is 0.784 A. The current estimated error of phase yb ranges from −2.273 A to 1.838 A, and the average current absolute error is 0.349 A. The current estimated error of phase yc ranges from −5.256 A to 7.675 A, and the average current absolute error is 0.555 A.

Fig. 14 shows the estimated current in the *y*-axis with adaptive current estimation. The current estimated error of phase ya is from −0.951 A to 2.036 A, and the average current absolute error is 0.172 A. The current estimated error of phase yb is from −1.157 A to 1.008 A, and the average current absolute error is 0.201 A. The current estimated error of phase yc is from −0.754 A to 0.673 A, and the average current absolute error is 0.086 A. Compared with the situation in which adaptive current estimation is not applied, the maximum errors of the current estimation of phases ya, yb, and yc are reduced by 67.6%, 73.5%, and 63.4%, respectively.

Fig. 15 shows the position estimation results in the y-axis without adaptive current estimation, and Fig. 16 shows the position estimation results when adaptive current estimation is used. Without adaptive current estimation, the position estimated error ranges from −7.119 mm to 6.896 mm, and the absolute position error is 3.372 mm on average. With adaptive current estimation, the position estimated error ranges from −2.365mm to 2.535 mm, and the absolute position error is 1.093 mm on average. Compared with the situation in which

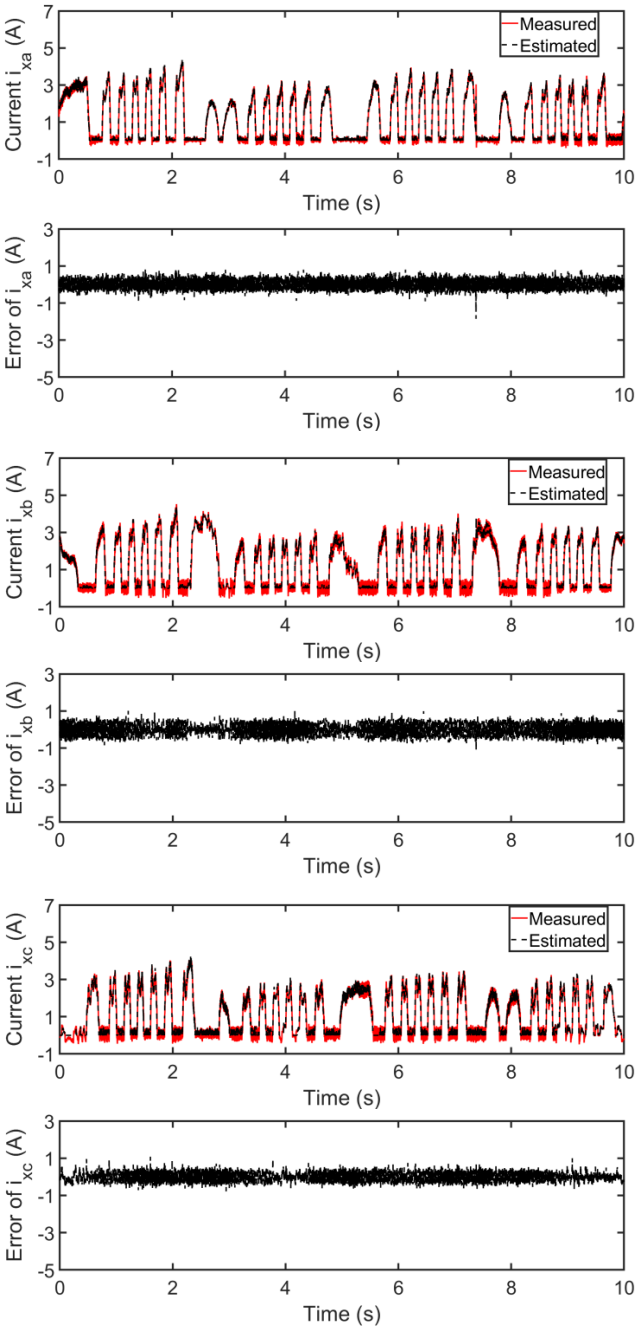


**FIGURE 10.** Estimated current results and estimated errors with the adaptive current estimation in the x-axis.

adaptive current estimation is not applied, the maximum error of the position estimation is reduced by 63.4%. Table 3 shows a detailed comparison of the errors in the estimated phase current $i_{lk}(l = \text{x, y}, k = \text{a, b, c})$ and the estimated position $s_l$ $(l = \text{x, y})$ in both cases with and without adaptive current estimation.

### C. ANALYSIS

Based on theoretical analysis and the experimental results, the factors that may lead to potential estimated errors are analyzed as follows.

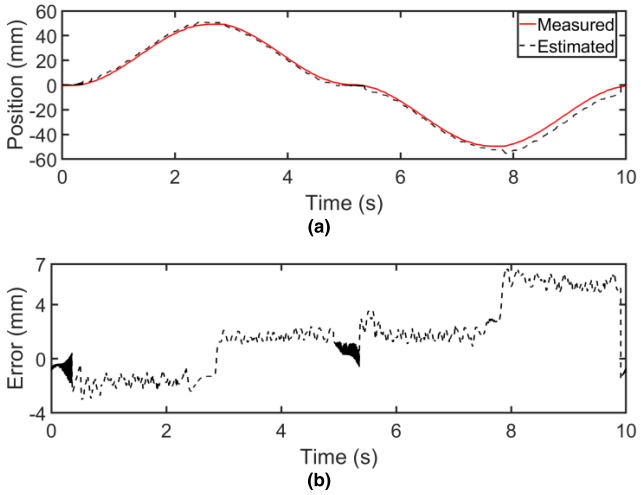


**FIGURE 11.** Estimated position results without adaptive current estimation in the x-axis: (a) Measured position and estimated position. (b) Estimated position error.

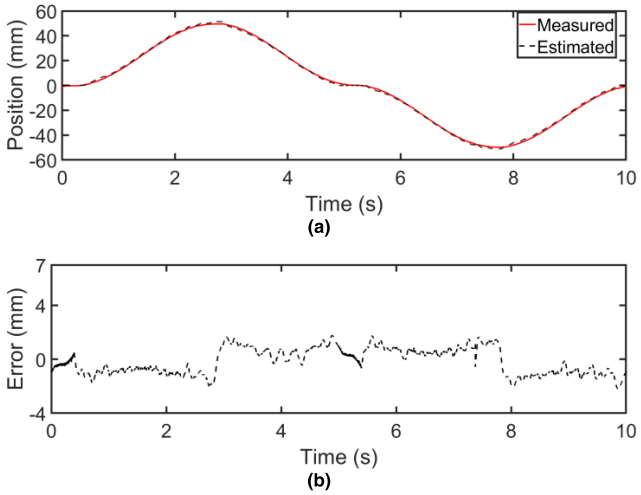


**FIGURE 12.** Estimated position results with the adaptive current estimation in the x-axis: (a) Measured position and estimated position. (b) Estimated position error.

#### 1) EFFECT OF THE MEASURED PHASE CURRENT AND VOLTAGE

In this paper, the phase current is measured by the interior current sensor of the motor drive, and the phase voltage is measured by the voltage isolation acquisition board. The offset and noise have been detected in these sensors. To minimize the offset and signal interference, an offset correction program and a low-pass filter with a cutoff frequency of 200 Hz are employed.

#### 2) EFFECT OF THE COIL RESISTANCE

The flux linkage is calculated by the integration of the phase current and voltage as discussed in (11), so the variation in the coil resistance will affect the estimation of the flux linkage. Due to the continuous operation of the PSRM, the temperature of the coil will increase [34], and the relationship

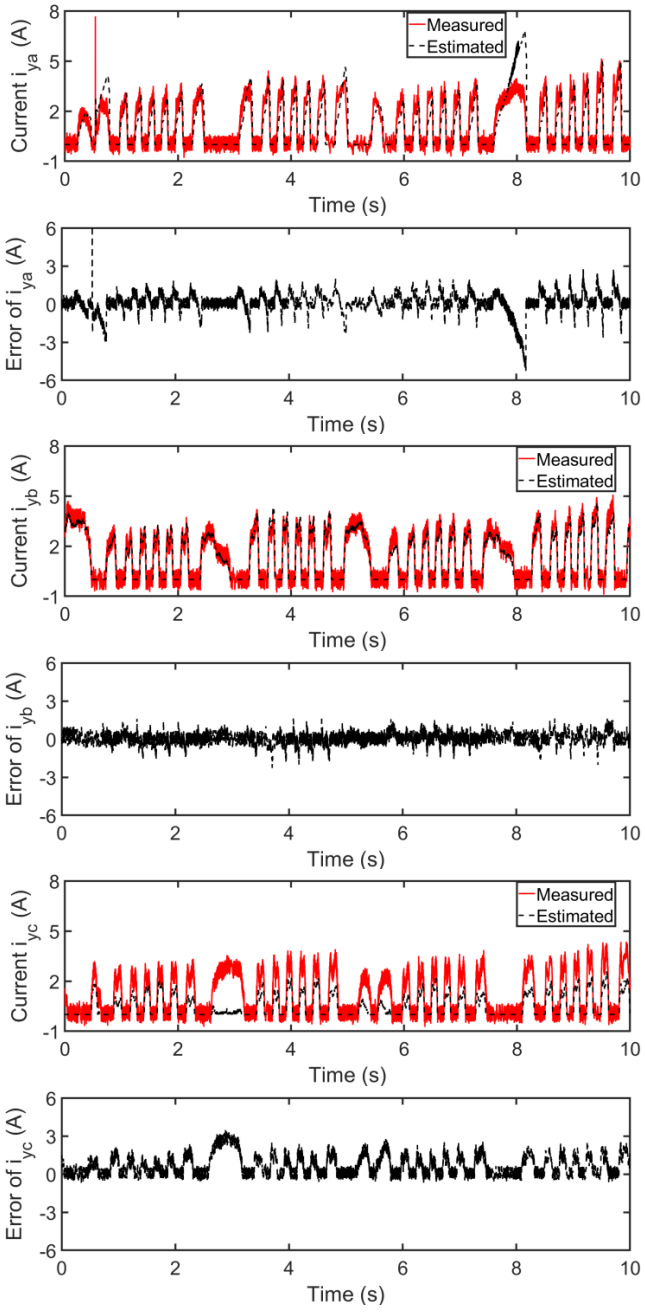


**FIGURE 13.** Estimated current results and estimated errors without adaptive current estimation in the y-axis.

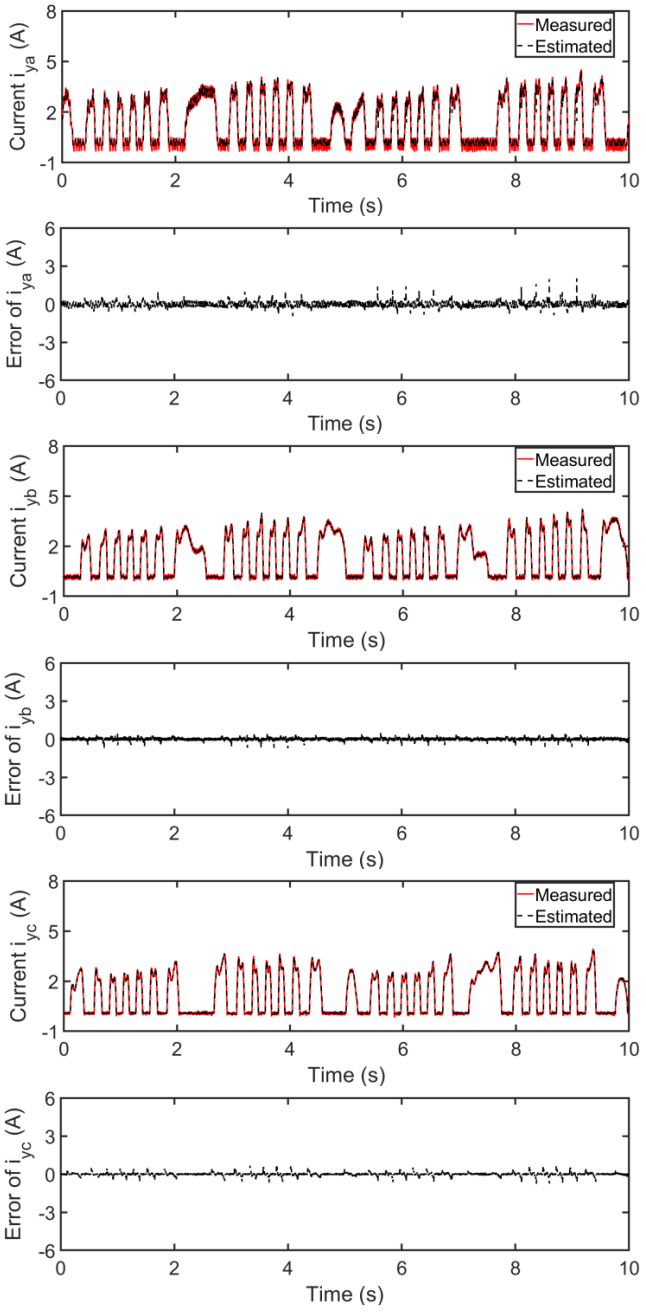


**FIGURE 14.** Estimated current results and estimated errors with the adaptive current estimation in the y-axis.

between the coil resistance and the temperature variation can be expressed as

$$R = R_0(1 + \alpha \Delta T/100) \tag{32}$$

where $\alpha$ is the temperature coefficient of the resistance, and $R_0$ is the resistance at $T_0$. In the proposed method, the flux linkage integration is cleared when the commutation is performed to reduce the accumulated error from the variation in the coil resistance in each electric period. The error caused by the temperature before the commutation cannot be eliminated by this method during every electric period. However, the electrical period is so small that the variation in the temperature in each period can be ignored. Therefore, the variation in the coil resistance in every electric period can also be ignored.

### 3) EFFECT OF THE PHASE INDUCTANCE

The average inductance $L_o$ and the inductance variation $L_\Delta$ in the inductance model used in (5) are not fixed values but vary with the mover position, which leads to estimated errors of the current. However, the adaptive current estimation in this paper can effectively reduce this error.

**TABLE 3.** Estimated error of the current and position.

| | Without adaptive current estimation | | With the adaptive current estimation | | Reduction in the maximum error |
|---|---|---|---|---|---|
| | Error | Average error | Error | Average error | |
| $i_{xa}$ | [-5.026, 2.339] A | 0.547 A | [-1.853, 0.867] A | 0.222 A | 63.1% |
| $i_{xb}$ | [-2.474, 1.746] A | 0.338 A | [-1.157, 1.008] A | 0.201 A | 59.3% |
| $i_{xc}$ | [-0.956, 3.176] A | 0.673 A | [-0.782, 1.080] A | 0.215 A | 66.0% |
| $s_x$ | [-3.014, 6.642] mm | 2.483 mm | [-2.239, 1.785] mm | 0.885 mm | 66.3% |
| $i_{ya}$ | [-0.742, 3.531] A | 0.784 A | [-0.951, 2.036] A | 0.172 A | 42.3% |
| $i_{yb}$ | [-2.273, 1.838] A | 0.349 A | [-0.736, 0.509] A | 0.092 A | 67.6% |
| $i_{yc}$ | [-5.256, 7.675] A | 0.555 A | [-0.754, 0.673] A | 0.086 A | 73.5% |
| $s_y$ | [-7.119, 6.896] mm | 3.372 mm | [-2.365, 2.535] mm | 1.093 mm | 63.4% |

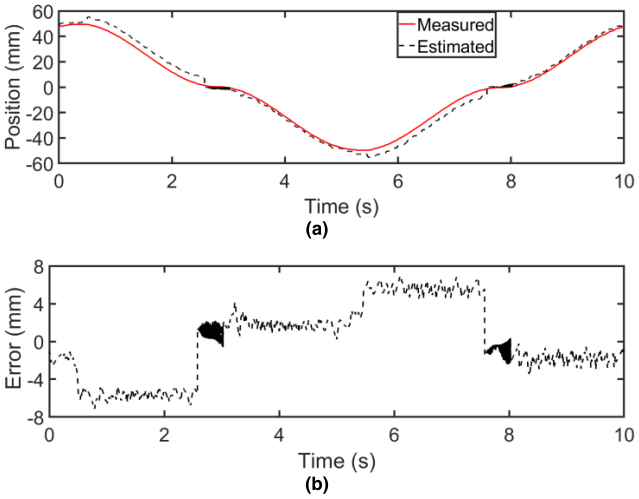


**FIGURE 15.** Estimated position results without adaptive current estimation in the y-axis: (a) Measured position and estimated position. (b) Estimated error.

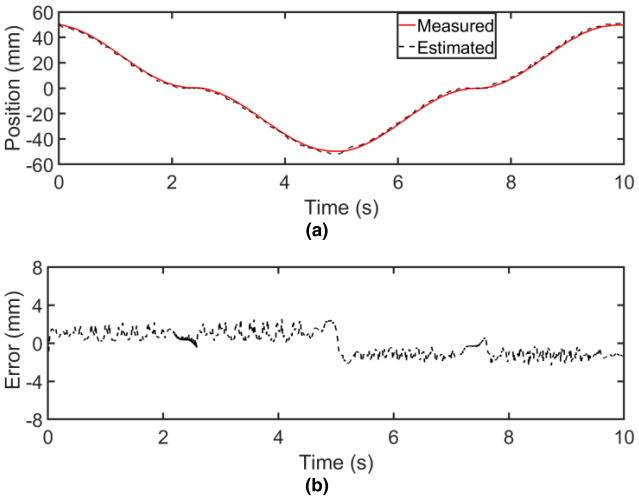


**FIGURE 16.** Estimated position results with the adaptive current estimation in the y-axis: (a) Measured position and estimated position. (b) Estimated error.

### 4) EFFECT OF THE MECHANICAL MODEL

It can be seen from (2) that the friction of the motor is not taken into account; however, the motor has a large normal force during operation in practice, which will generate friction in the horizontal direction, so the estimation of the mover acceleration $\dot{v}_l$ is not accurate enough. The estimated position is obtained by the integration of the mover speed $v_l$, which is the integration of $\dot{v}_l$. In this process, the integration accumulates the errors of the mover position. In response to this problem, a position and speed correction module was developed to clear the estimated position. The module clears the value of the estimated position when the reference position of the mover is judged to be 0 mm. Similarly, the estimated speed is cleared when the reference speed is judged to be 0 m/s to clear the accumulated error in the integration process.

## V. CONCLUSION

This paper presents the first attempt to comprehensively report sensorless control for a PSRM. The SMO-based position estimation method for sensorless control of a PSRM has been proposed. The mover position is estimated by detecting the voltage and current of every phase. The experimental results indicate that the errors of the current and position are greatly reduced by using adaptive current estimation, and the mean absolute error of the estimated position is 0.885 mm in the x-axis and 1.093 mm in the y-axis, respectively. It can be concluded that the proposed method is feasible for a PSRM without employing a position sensor. This method requires neither additional hardware, nor massive experimental data, nor huge interior memory. Furthermore, this method has the advantage of generating no opposite force without an injected pulse. The imprecise mechanical model that does not consider friction, which is applied to develop the SMO, is the main source of the position error. Future work will focus on an accurate mechanical model considering friction to improve the accuracy of the estimated position.

## REFERENCES

[1] J. M. M. Rovers, J. W. Jansen, J. C. Compter, and E. A. Lomonova, "Analysis method of the dynamic force and torque distribution in the magnet array of a commutated magnetically levitated planar actuator," *IEEE Trans. Ind. Electron.*, vol. 59, no. 5, pp. 2157–2166, May 2012.

[2] L. Zhang, B. Kou, L. Li, and B. Zhao, "Modeling and design of an integrated winding synchronous permanent magnet planar motor," *IEEE Trans. Plasma Sci.*, vol. 41, no. 5, pp. 1214–1219, May 2013.

[3] J. W. Jansen, J. P. C. Smeets, T. T. Overboom, J. M. M. Rovers, and E. A. Lomonova, "Overview of analytical models for the design of linear and planar motors," *IEEE Trans. Magn.*, vol. 50, no. 11, Nov. 2014, Art. no. 8206207.

[4] M.-Y. Chen, H.-H. Huang, and S.-K. Hung, "A new design of a submicropositioner utilizing electromagnetic actuators and flexure mechanism," *IEEE Trans. Ind. Electron.*, vol. 57, no. 1, pp. 96–106, Jan. 2010.
[5] J. Pan, N. C. Cheung, and J. Yang, "High-precision position control of a novel planar switched reluctance motor," *IEEE Trans. Ind. Electron.*, vol. 52, no. 6, pp. 1644–1652, Dec. 2005.
[6] S.-D. Huang *et al.*, "Maximum-force-per-ampere strategy of current distribution for efficiency improvement in planar switched reluctance motors," *IEEE Trans. Ind. Electron.*, vol. 63, no. 3, pp. 1665–1675, Mar. 2016.
[7] S. D. Huang, G. Z. Cao, Z. Y. He, J. F. Pan, J. A. Duan, and Q. Q. Qian, "Nonlinear modeling of the inverse force function for the planar switched reluctance motor using sparse least squares support vector machines," *IEEE Trans. Ind. Informat.*, vol. 11, no. 3, pp. 591–600, Jun. 2015.
[8] G.-Z. Cao, L.-L. Li, S.-D. Huang, L.-M. Li, Q.-Q. Qian, and J.-A. Duan, "Nonlinear modeling of electromagnetic forces for the planar-switched reluctance motor," *IEEE Trans. Magn.*, vol. 51, no. 11, Nov. 2015, Art. no. 8206605.
[9] J. F. Pan and N. C. Cheung, "An adaptive controller for the novel planar switched reluctance motor," *IET Electr. Power Appl.*, vol. 5, no. 9, pp. 677–683, Nov. 2011.
[10] G.-Z. Cao, S.-S. Xiao, S.-D. Huang, Z.-M. Chen, and D.-L. Liang, "Sensorless position detection of the planar switched reluctance motor using the current injection method," in *Proc. IEMDC*, Miami, FL, USA, 2017, pp. 1–6.
[11] M. Ehsani and B. Fahimi, "Elimination of position sensors in switched reluctance motor drives: State of the art and future trends," *IEEE Trans. Ind. Electron.*, vol. 49, no. 1, pp. 40–47, Feb. 2002.
[12] E. Ofori, T. Husain, Y. Sozer, and I. Husain, "A pulse-injection-based sensorless position estimation method for a switched reluctance machine over a wide speed range," *IEEE Trans. Ind. Appl.*, vol. 51, no. 5, pp. 3867–3876, Sep./Oct. 2015.
[13] M. Ehsani, I. Husain, S. Mahajan, and K. R. Ramani, "New modulation encoding techniques for indirect rotor position sensing in switched reluctance motors," *IEEE Trans. Ind. Appl.*, vol. 30, no. 1, pp. 85–91, Jan. 1994.
[14] E. Afjei, M. Asgar, A. Kamrani, and M. S. Afjei, "Rotor position estimation of switched reluctance motors based on digital amplitude technique," in *Proc. SPEEDAM*, Anacapri, Italy, 2016, pp. 505–509.
[15] P. P. Acarnley, R. J. Hill, and C. W. Hooper, "Detection of rotor position in stepping and switched motors by monitoring of current waveforms," *IEEE Trans. Ind. Electron.*, vol. IE-32, no. 3, pp. 215–222, Aug. 1985.
[16] G. Gallegos-Lopez, P. C. Kjaer, and T. J. E. Miller, "A new sensorless method for switched reluctance motor drives," *IEEE Trans. Ind. Appl.*, vol. 34, no. 4, pp. 832–840, Jul. 1998.
[17] F. R. Salmasi, B. Fahimi, H. Gao, and M. Ehsani, "Sensorless control of switched reluctance motor drive based on BEMF calculation," in *Proc. IEEE Appl. Power Electron. Conf.*, Dallas, TX, USA, Mar. 2002, pp. 293–298.
[18] H.-Y. Yang, J.-H. Kim, and R. Krishnan, "Low-cost position sensorless switched relutance motor drive using a single-controllable switch converter," *J. Power Electron.*, vol. 12, pp. 75–82, Jan. 2012.
[19] Q. Wang, H. Chen, T. Xu, R. Nie, J. Wang, and S. Abbas, "Position estimation of linear switched reluctance machine with iron losses based on eddy-current effect," *IET Electr. Power Appl.*, vol. 10, no. 8, pp. 772–778, Sep. 2016.
[20] J. P. Lyons, S. R. Macminn, and M. A. Preston, "Flux-current methods for SRM rotor position estimation," in *Proc. Conf. Rec. IEEE-IAS Annu. Meeting*, Dearborn, MI, USA, Sep./Oct. 1991, pp. 482–487.
[21] M. Polat, E. Oksuztepe, and H. Kurum, "Switched reluctance motor control without position sensor by using data obtained from finite element method in artificial neural network," *Elect. Eng.*, vol. 98, no. 1, pp. 43–54, Mar. 2016.
[22] C. A. Hudson, N. S. Lobo, and R. Krishnan, "Sensorless control of single switch-based switched reluctance motor drive using neural network," *IEEE Trans. Ind. Electron.*, vol. 55, no. 1, pp. 321–329, Jan. 2008.
[23] N. Ertugrul and A. D. Cheok, "Indirect angle estimation in switched reluctance motor drive using fuzzy logic based motor model," *IEEE Trans. Power Electron.*, vol. 15, no. 6, pp. 1029–1044, Nov. 2000.
[24] Y. Zou, K. W. E. Cheng, N. C. Cheung, and J. F. Pan, "A polymer-based air gap length prediction method with current injection and fuzzy logic observer," *IEEE Trans. Magn.*, vol. 53, no. 11, Nov. 2017, Art. no. 2002404.
[25] A. Lumsdaine and J. H. Lang, "State observers for variable-reluctance motors," *IEEE Trans. Ind. Electron.*, vol. 37, no. 2, pp. 133–142, Apr. 1990.
[26] M. S. Zaky, M. K. Metwaly, H. Z. Azazi, and S. A. Deraz, "A new adaptive smo for speed estimation of sensorless induction motor drives at zero and very low frequencies," *IEEE Trans. Ind. Electron.*, vol. 65, no. 9, pp. 6901–6911, Sep. 2018.
[27] Y. Saadi, R. Sehab, A. Chaibet, M. Boukhnifer, and D. Diallo, "Sensorless control of switched reluctance motor for EV application using a sliding mode observer with unknown inputs," in *Proc. ICIT*, Lyon, France, 2018, pp. 516–521.
[28] L. Shen, J. Wu, S. Yang, and X. Huang, "Fast flux linkage measurement for switched reluctance motors excluding rotor clamping devices and position sensors," *IEEE Trans. Instrum. Meas.*, vol. 62, no. 1, pp. 185–191, Jan. 2013.
[29] R. Krishnan, *Switched Reluctance Motor Drives: Modeling, Simulation, Analysis, Design, and Applications*. Boca Raton, FL, USA: CRC Press, 2001.
[30] L. Sheng, W. Li, Y. Wang, M. Fan, and X. Yang, "Sensorless control of a shearer short-range cutting interior permanent magnet synchronous motor based on a new sliding mode observer," *IEEE Access*, vol. 5, pp. 18439–18450, 2017.
[31] I. Husain, S. Sodhi, and M. Ehsani, "A sliding mode observer based controller for switched reluctance motor drives," in *Proc. Conf. Rec. IEEE-IAS Annu. Meeting*, Denver, CO, USA, Oct. 1994, pp. 635–643.
[32] C. Yang, T. Ma, Z. Che, and L. Zhou, "An adaptive-gain sliding mode observer for sensorless control of permanent magnet linear synchronous motors," *IEEE Access*, vol. 6, pp. 3469–3478, 2018.
[33] R. A. McCann, M. S. Islam, and I. Husain, "Application of a sliding-mode observer for position and speed estimation in switched reluctance motor drives," *IEEE Trans. Ind. Appl.*, vol. 37, no. 1, pp. 51–58, Jan. 2001.
[34] J. Cai and Z. Deng, "Initial rotor position estimation and sensorless control of SRM based on coordinate transformation," *IEEE Trans. Instrum. Meas.*, vol. 64, no. 4, pp. 1004–1018, Apr. 2015.

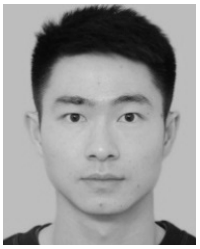

**JUNDI SUN** (S'17) received the M.Sc. degree in control theory and control engineering from Shenzhen University, Shenzhen, China, in 2017. He is currently pursuing the joint Ph.D. degree in electrical engineering with Southwest Jiaotong University, Chengdu, China, and the Shenzhen Key Laboratory of Electromagnetic Control, Shenzhen University. His research interests include the design and control of planar switched reluctance motors, and sensorless control.

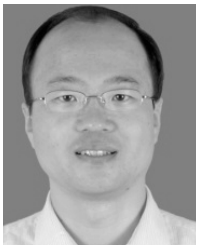

**GUANG-ZHONG CAO** (M'15–SM'17) received the B.Sc., M.Sc., and Ph.D. degrees from Xi'an Jiaotong University, Xi'an, China, in 1989, 1992, and 1996, respectively, all in electrical engineering and automation. He is currently a Professor and the Director of the Shenzhen Key Laboratory of Electromagnetic Control, College of Mechatronics and Control Engineering, Shenzhen University, China. He has authored more than 100 articles in refereed journals and conference proceedings. His research interests include control theory, motor control, robotics and the Internet of Things.

**SU-DAN HUANG** (M'17) received the B.Sc. and M.Sc. degrees in control theory and control engineering from Shenzhen University, Shenzhen, China, in 2009 and 2012, respectively, and the Ph.D. degree in electrical engineering from Southwest Jiaotong University, Chengdu, China, in 2016. She is currently an Assistant Professor with the Shenzhen Key Laboratory of Electromagnetic Control, College of Mechatronics and Control Engineering, Shenzhen University, China. Her research interests include the design and control of planar switched reluctance motors, magnetic levitation systems, and control theory and its applications.

**YEPING PENG** (M'18) received the B.Sc. degree in mechanical design, manufacture and automation from Harbin Engineering University, Harbin, China, the M.Sc. and Ph.D. degrees in mechanical engineering from Xi'an Jiaotong University, Xi'an, China, in 2011, 2014, and 2017, respectively. She is currently an Assistant Professor with the Shenzhen Key Laboratory of Electromagnetic Control, College of Mechatronics and Control Engineering, Shenzhen University, China. Her main research interests include machine vision, image processing, and signal processing.

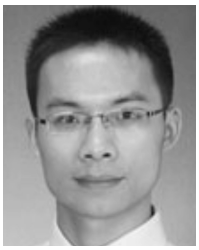

**JIANGBIAO HE** (S'08–M'15–SM'16) received the Ph.D. degree in electrical engineering with an emphasis on power energy conversion from Marquette University, Milwaukee, WI, USA, in 2015.

Most recently, he was a Lead Engineer at GE Global Research, Niskayuna, NY, USA. He was also with Eaton Corporate Research and Technology and Rockwell Automation before joined GE, in 2015. He is currently an Assistant Professor with the Department of Electrical and Computer Engineering, University of Kentucky, USA. His research interests include high-power high-frequency propulsion drives for electric transportation, renewable energy power conversion, and fault-tolerant operation of power conversion systems for safety-critical applications. He has authored or coauthored more than 50 technical papers and 10 patent applications in power electronics and motor drives areas.

Dr. He has served as an Associate Editor for several prestigious IEEE journals in electric power area. He has also served as the Secretary of the Standards Sub-committee for IEEE Industrial Drives group and an Organizing Committee Member on several large international conferences, including ECCE-2018, IEMDC-2019, and ITEC-2019.

**QING-QUAN QIAN** received the B.Sc. degree in electrical engineering from Southwest Jiaotong University, Chengdu, China, in 1960. Since 1997, he has been an Academician with the Chinese Academy of Engineering, Beijing, China. He is currently a Professor with the Department of Electrical Engineering, Southwest Jiaotong University. His research interests include electrification and automation of rail transit.